

# Full three dimensional cavitation instabilities using a non-quadratic anisotropic yield function

**Legarth, Brian Nyvang; Tvergaard, Viggo**

*Published in:*
Journal of Applied Mechanics

*Link to article, DOI:*
10.1115/1.4044955

*Publication date:*
2020

*Document Version*
Peer reviewed version

Journal of Applied Mechanics. Received July 10, 2019;
Accepted manuscript posted September 20, 2019. doi:10.1115/1.4044955


# Full three dimensional cavitation instabilities using a non-quadratic anisotropic yield function

Brian Nyvang Legarth* and Viggo Tvergaard

Department of Mechanical Engineering, Solid Mechanics, Technical University of Denmark
DK-2800 Kgs. Lyngby, Denmark

*Corresponding author: bnl@mek.dtu.dk

**Abstract**

Full three dimensional cell models containing a small cavity are used to study the effect of plastic anisotropy on cavitation instabilities. Predictions for the Barlat-91 model (Int. J. Plast. **7**, 693-712, 1991), with a non-quadratic anisotropic yield function, are compared with previous results for the classical anisotropic Hill-48 quadratic yield function (Proc. Royal Soc. Lond. **A193**, 281-297, 1948). The critical stress, at which the stored elastic energy will drive the cavity growth, is strongly affected by the anisotropy as compared to isotropic plasticity, but does not show much difference between the two models of anisotropy. While a cavity tends to remain nearly spherical during a cavitation instability in isotropic plasticity, the cavity shapes in an anisotropic material develop towards near-spheroidal elongated shapes, which differ for different values of the coefficients defining the anisotropy. The shapes found for the Barlat-91 model, with a non-quadratic anisotropic yield function, differ noticeably from the shapes found for the quadratic Hill-48 yield function. Computations are included for a high value of the exponent in the Barlat-91 model, where this model represents a Tresca-like yield surface with rounded corners.

**Keywords**: Non-quadratic anisotropic plasticity, finite deformations, cavity shape, cavitation instability.

## 1 Introduction

For a single cavity in an infinite elastic-plastic solid under tensile loading a cavitation instability is found, if the stress level and the stress triaxiality are so high that the work released in the fields around the growing cavity can drive continued expansion. The phenomenon has been studied by Hill and coauthors [1, 2] for spherically symmetric conditions, and has also been found for spherical cavities subject to more general axisymmetric conditions when the remote hydrostatic tension is sufficiently high [3,4]. The influence of initially spheroidal cavities, either prolate or oblate, has been considered by Tvergaard and Hutchinson [5], who found that for a standard $J_2$ flow theory material these cavities rapidly approached a spherical shape during cavity growth, so that after some growth there is little difference from an initially spherical cavity. However, in the case of anisotropic plasticity it has recently been found (Tvergaard and Legarth [6]) that the final cavity shape develops towards a spheroidal shape, even if the cavity is initially spherical, and even if the macroscopic stress state is spherically symmetric.

Stress levels sufficiently high to result in a cavitation instability can be reached in metal-ceramic systems, where the constraint on plastic flow in the metal tends to give high stress triaxiality. Thus, for a thin metal layer bonding two ceramic blocks Dalgleish et al. [7] have observed rapid cavity growth under tension normal to the layer. For a ceramic reinforced by Al particles a single dominant cavity has been observed in some of the particles crossed by a fracture surface (Flinn et al. [8]), and similar observations have been made in model experiments (Ashby et al. [9]). Also in a metal matrix composite reinforced by ceramic fibres a cavitation instability can occur in the metal between fibre ends, dependent on the material parameters (Tvergaard [10]).

Unstable cavity growth has also been studied for non-linear elasticity (Ball [11], Horgan and Abeyarathne [12], Horgan and Poligone [13]) where a cavitation instability has been interpreted either as a bifurcation from a homogeneously stressed solid with no cavity to a solid containing a cavity, or as the growth of a pre-existing cavity.

The analyses of Tvergaard and Legarth [6] were numerical studies for a full 3D cell model, as needed in order to find the cavity shapes that develop during the unstable growth. Here the plastic anisotropy was represented by the classical anisotropic quadratic yield function, subsequently denoted Hill-48 [2, 14]. The purpose of the present study is to investigate the effect on cavitation instabilities when a different anisotropic plasticity model is used. The yield function considered is proposed by Barlat et *al.* [15], here denoted Barlat-91, which allows for a non-quadratic expression, with an exponent $d$ in the yield function. For $d = 8$ the coefficients in this yield function are calculated such that three selected uniaxial tensile tests ($0^o, 45^o$ and $90^o$) agree with those used in the studies [6] based on Hill-48. Furthermore, the effect of using a higher exponent, $d = 14$, is considered. For these material values it is found that the values of the critical stresses are not much affected by the different anisotropic plasticity model. But there is a noticeable influence on the cavity shapes that develop.

The present studies also include analyses where the main tensile direction relative to the principal directions of the anisotropy are different from those considered in [6]. Furthermore, a computation is included for a high value

Journal of Applied Mechanics. Received July 10, 2019;
Accepted manuscript posted September 20, 2019. doi:10.1115/1.4044955


of the exponent $d$, where the Barlat-91 model represents a Tresca-like yield surface with rounded corners.

## 2 Material Model

The elasto-plastically anisotropic material model used accounts for small elastic but finite plastic deformations. The elastic deformations are assumed to be linearly isotropic and governed by Hooke's law through Young's modulus, $E$, and Poisson's ratio, $\nu$.

The time derivatives with respect to time, $t$, are denoted by a superposed dot. The components of the second-order velocity gradient tensor, $\mathbf{L}$, are then determined by $L_{ij} = \frac{\partial \dot{u}_i}{\partial x_j} = \dot{u}_{i,j}$, where the velocity field components for the material are $\dot{u}_i$ and $u_i$ is the displacement field. The symmetric part of $\mathbf{L}$ is the strain rate, $\mathbf{D}$, and the antisymmetric part is the continuum spin tensor, $\omega$, such that [16–18]

$$\mathbf{L} = \mathbf{D} + \omega \quad ; \quad \mathbf{D} = \mathbf{D}^{\mathrm{e}} + \mathbf{D}^{\mathrm{p}} \tag{1}$$

where the superscripts e and p denote the elastic and plastic parts, respectively. The objective rate with respect to $\omega$, $\overset{\triangledown}{(\,)}$, of the symmetric Kirchhoff stress, $\tau$, is introduced as [19]

$$\overset{\triangledown}{\tau} = \mathbf{C} : \mathbf{D}^{\mathrm{e}} = \mathbf{C} : (\mathbf{D} - \mathbf{D}^{\mathrm{p}}) \tag{2}$$

Here, $\mathbf{C}$ are the isotropic elastic moduli determined by $E$ and $\nu$. The plastic strain rates, $\mathbf{D}^{\mathrm{p}}$, are formulated in a visco-plastic setting as

$$\mathbf{D}^{\mathrm{p}} = \dot{\phi}\mathbf{N}^{\mathrm{p}} \quad ; \qquad \dot{\phi} = \dot{\varepsilon}_0 \left(\frac{J}{g}\right)^{1/m} \quad ; \qquad \mathbf{N}^{\mathrm{p}} = \frac{\partial J}{\partial \sigma} \tag{3}$$

where the magnitude of the effective plastic strain rate is denoted $\dot{\phi}$ and $\mathbf{N}^{\mathrm{p}}$ are the normals to the yield surface formulated in terms of the symmetric Cauchy stress tensor, $\sigma$, which then gives the direction of the plastic strain increments, $\mathbf{D}^{\mathrm{p}}$. The reference strain rate is $\dot{\varepsilon}_0$, $m$ is a strain rate sensitivity parameter, $g$ is a deformation dependent power-law hardening function and $J$ is the value of the effective stress according to a yield function.

For comparison, a few results will be given using the classical anisotropic quadratic yield function proposed by Hill [2, 14], subsequently denoted as Hill-48. However, the main focus here is the non-quadratic anisotropic yield function proposed by Barlat et al. [15], which subsequently will be denoted Barlat-91. A comparison study of Hill-48 and Barlat-91 as well as two more yield surfaces can be found in elsewhere [20]. The effective stress of Barlat-91 is evaluated as $J = (\Phi/2)^{1/d}$ with

$$\Phi = [S_1 - S_2]^d + [S_2 - S_3]^d + [S_1 - S_3]^d \tag{4}$$

where the exponent $d$ is typically eight for FCC-crystal structures, but is generally yet another fitting parameter. Also

$$\begin{aligned} S_1 &= 2\sqrt{I_2}\cos\left(\frac{\bar{\theta}}{3}\right) \\ S_2 &= 2\sqrt{I_2}\cos\left(\frac{\bar{\theta}-2\pi}{3}\right) \\ S_3 &= 2\sqrt{I_2}\cos\left(\frac{\bar{\theta}+2\pi}{3}\right) \end{aligned} \tag{5}$$

$$\begin{aligned} I_2 = {} & \tfrac{1}{3}\left[(\bar{f}\bar{F})^2 + (\bar{g}\bar{G})^2 + (\bar{h}\bar{H})^2\right] \\ & + \tfrac{1}{54}\left[(\bar{a}\bar{A} - \bar{c}\bar{C})^2 + (\bar{c}\bar{C} - \bar{b}\bar{B})^2 + (\bar{b}\bar{B} - \bar{a}\bar{A})^2\right] \\ I_3 = {} & \tfrac{1}{54}\left[(\bar{c}\bar{C} - \bar{b}\bar{B})(\bar{a}\bar{A} - \bar{c}\bar{C})(\bar{b}\bar{B} - \bar{a}\bar{A})\right] + \bar{f}\bar{g}\bar{h}\bar{F}\bar{G}\bar{H} \\ & - \tfrac{1}{6}\left[(\bar{c}\bar{C} - \bar{b}\bar{B})(\bar{f}\bar{F})^2 + (\bar{a}\bar{A} - \bar{c}\bar{C})(\bar{g}\bar{G})^2 \right. \\ & \left. + (\bar{b}\bar{B} - \bar{a}\bar{A})(\bar{h}\bar{H})^2\right] \end{aligned} \tag{6}$$

$$0 \le \bar{\theta} = \arccos\left(\frac{I_3}{I_2^{3/2}}\right) \le \pi \tag{7}$$

with

$$\begin{aligned} \bar{A} &= \hat{\sigma}_{22} - \hat{\sigma}_{33} \quad ; \quad \bar{F} = \hat{\sigma}_{23} \\ \bar{B} &= \hat{\sigma}_{33} - \hat{\sigma}_{11} \quad ; \quad \bar{G} = \hat{\sigma}_{31} \\ \bar{C} &= \hat{\sigma}_{11} - \hat{\sigma}_{22} \quad ; \quad \bar{H} = \hat{\sigma}_{12} \end{aligned} \tag{8}$$

The superposed hat denotes stresses referring to the principal axes of anisotropy, which will further be described later. For $\bar{\theta} = 0$ or $\bar{\theta} = \pi$ in Eq. (7) the derivatives in Eq. (3) are singular. For these particular cases Eq. (4) reduces to

$$\Phi = 2 \cdot 3^d I_2^{\frac{d}{2}} \qquad \text{for } \bar{\theta} = 0 \quad \text{or} \quad \bar{\theta} = \pi \tag{9}$$

which are then directly used to evaluate the strain increments. If the coefficients of anisotropy, $\bar{a}, \bar{b}, \bar{c}, \bar{f}, \bar{g}$ and $\bar{h}$, are chosen to be unity and the exponent is $d = 2$ or $d \gg 2$, this criterion reduces to the isotropic Mises yield function or an isotropic Tresca-like yield function with rounded corners, respectively.

The deformation dependent hardening function, $g$ in Eq. (3), is taken as $g(\varepsilon^{\mathrm{p}}) = \sigma_0\,(1 + \varepsilon^{\mathrm{p}}/\varepsilon_0)^n$ where $\sigma_0$ is the initial uniaxial yield stress in the $x_1$ direction, $\varepsilon_0 = \sigma_0/E$, $n$ is the hardening exponent and the accumulated effective plastic strain, $\varepsilon^{\mathrm{p}}$, is

$$\varepsilon^{\mathrm{p}} = \int \dot{\varepsilon}^{\mathrm{p}}\,\mathrm{d}t \quad ; \qquad \dot{\varepsilon}^{\mathrm{p}} = \dot{\phi}\sqrt{\frac{2}{3}\,\mathbf{N}^{\mathrm{p}} : \mathbf{N}^{\mathrm{p}}} \tag{10}$$

The deformation history will be calculated in a linear incremental manner. In order to increase the stable time step,

Journal of Applied Mechanics. Received July 10, 2019;
Accepted manuscript posted September 20, 2019. doi:10.1115/1.4044955


$\Delta t$, the rate tangent modulus method is used [21]. This is a forward gradient method based on an estimate of the plastic strain rate in the interval between $t$ and $t+\Delta t$ defined by $\rho \in [0;1]$. The time step for the next increment is adaptively adjusted according to $(\dot{\varepsilon}^{\mathrm{p}})_{\max} \cdot \Delta t \leq 10^{-5}$, where $(\dot{\varepsilon}^{\mathrm{p}})_{\max}$ is the maximum effective plastic strain rate in any material point.

The final form of the constitutive relations can then be written as [19, 22]

$$\dot{\sigma} = \overset{\triangledown}{\tau} + \omega\sigma + \sigma\omega - \sigma\,\mathrm{tr}(\mathbf{D}) \tag{11}$$

with

$$\begin{aligned}
&\overset{\triangledown}{\tau} = \tilde{\mathbf{C}} : \mathbf{D} - \mathbf{P} \\
&\tilde{\mathbf{C}} = \mathbf{C} - \tfrac{\xi}{h(1+\xi)} (\mathbf{C} : \mathbf{N}^{\mathrm{p}}) \otimes (\mathbf{N}^{\mathrm{p}} : \mathbf{C}) \\
&\mathbf{P} = \tfrac{\dot{\phi}_t}{1+\xi} (\mathbf{C} : \mathbf{N}^{\mathrm{p}}) \\
&\xi = \rho \Delta t \left( \tfrac{\partial \dot{\phi}}{\partial J} \right)_t h \quad ; \qquad \rho \in [0;1] \\
&h = \mathbf{N}^{\mathrm{p}} : \mathbf{C} : \mathbf{N}^{\mathrm{p}} - \left( \tfrac{\partial \dot{\phi}}{\partial \varepsilon^{\mathrm{p}}} \right)_t \left( \tfrac{\partial \dot{\phi}}{\partial J} \right)_t^{-1} \sqrt{\tfrac{2}{3}}
\end{aligned} \tag{12}$$

where the subscript $t$ denotes that the derivatives are taken at the start of the increment. Throughout the paper $\rho = 1$ will be used. It is noted, that $\mathrm{tr}(\mathbf{D}) = \mathrm{tr}(\mathbf{D}^{\mathrm{e}}) \simeq 0$ due to plastic incompressibility where $\mathrm{tr}(\mathbf{D}^{\mathrm{p}}) = \mathrm{tr}(\mathbf{N}^{\mathrm{p}}) \equiv 0$.

## 3 Problem Formulation and Numerical Procedure

The spheroidal cavity studied is illustrated in Fig. 1, where the cavity is highly magnified as the initial cavity volume fraction in the computations is taken to be $5 \cdot 10^{-7}$ (corresponding to $a_2/L_2 \simeq 0.01$ for an initially spherical cavity). The shape is defined by the three initial half axes, $a_1, a_2$ and $a_3$, aligned with the sides of the cell. The cavity shape will subsequently be characterized by $w_1 = a_2/a_1$ and $w_3 = a_2/a_3$. Fig. 1 also shows the reference Cartesian coordinate axes used, $x_i$, which are aligned with the sides of the domain analyzed. The load is characterized by the three average true normal stress components, $\Sigma_1, \Sigma_2$ and $\Sigma_3$, acting in the three coordinate directions, $x_i$ (load not shown in Fig. 1). Taking $x_2$ as the primary loading direction, the stress components are related such that $\Sigma_1 = \kappa_1 \Sigma_2$ and $\Sigma_3 = \kappa_3 \Sigma_2$, where $\kappa_1$ and $\kappa_3$ are prescribed ratios. The boundary conditions are expressed in terms of the displacement rates, $\dot{u}_i$, and the surface traction rates, $\dot{T}_i$, as

$$\begin{array}{lcllll}
\dot{u}_1 = 0 & ; & \dot{T}_2 = \dot{T}_3 = 0 & \text{at} & x_1 = 0 \\
\dot{u}_2 = 0 & ; & \dot{T}_1 = \dot{T}_3 = 0 & \text{at} & x_2 = 0 \\
\dot{u}_3 = 0 & ; & \dot{T}_1 = \dot{T}_2 = 0 & \text{at} & x_3 = 0 \\
\dot{u}_1 = \Delta_1 & ; & \dot{T}_2 = \dot{T}_3 = 0 & \text{at} & x_1 = L_1 \\
\dot{u}_2 = \Delta_2 & ; & \dot{T}_1 = \dot{T}_3 = 0 & \text{at} & x_2 = L_2 \\
\dot{u}_3 = \Delta_3 & ; & \dot{T}_1 = \dot{T}_2 = 0 & \text{at} & x_3 = L_3
\end{array} \tag{13}$$

where $\Delta_1, \Delta_2$ and $\Delta_3$ are prescribed displacement quantities used to introduce the load at the external deformed boundary

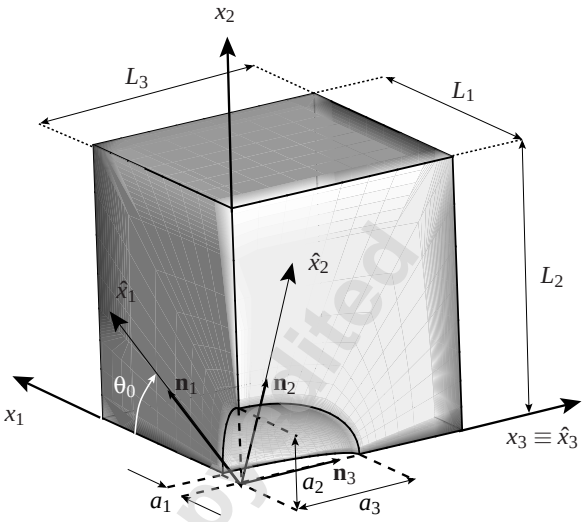


Fig. 1. Geometry of spheroidal cavity with coordinate systems. Illustrated for $w_1 = a_2/a_1 = 2.0$ and $w_3 = a_2/a_3 = \frac{1}{2}$ as well as $L_2/L_1 = L_2/L_3 = 1.0$.

given by $L_1, L_2$ and $L_3$, see Fig. 1. To impose the stress ratios, $\kappa_1$ and $\kappa_3$, the stresses are first evaluated for $\Delta_1, \Delta_2$ and $\Delta_3$ separately. Then the $\Delta$-values giving the required stress ratios are calculated by using the combined finite element and Rayleigh-Ritz procedure as proposed by Tvergaard [23]. Another possible method has been proposed in [24].

The principal axes of anisotropy, $\hat{x}_i$, with the orthogonal base vectors $\mathbf{n}_i$ are also depicted in Fig. 1. They are shown for an initial angle, $\theta_0$, rotated around the $x_3$-axis alone, such that $x_3 \equiv \hat{x}_3$. The initial base vectors can then be given as

$$\mathbf{n}_1 = \left\{ \begin{array}{c} \cos(\theta_0) \\ \sin(\theta_0) \\ 0 \end{array} \right\} \quad \mathbf{n}_2 = \left\{ \begin{array}{c} -\sin(\theta_0) \\ \cos(\theta_0) \\ 0 \end{array} \right\} \quad \mathbf{n}_3 = \left\{ \begin{array}{c} 0 \\ 0 \\ 1 \end{array} \right\} \tag{14}$$

where the instantaneous orientation is given by the evolution law $\dot{\mathbf{n}}_i = \omega \mathbf{n}_i$. No remote shear loads will be applied to the cell sides and for $\theta_0 = 0^o$ and $\theta_0 = 90^o$ this then leads to no rotation of $\mathbf{n}_i$ at the sides. Within the interior of the cell shear stresses may develop throughout the load history, and rotations may occur. However, symmetries along the boundaries will remain and only one-eighth of the unit cell needs to be analyzed even for the spheroidal cavity. In general cases, periodical boundary conditions on a cell containing the full cavity is needed, leading to a heavily increased computational effort as eight times as many elements are needed in addition to a large number of Multiple-Point-Constraints destroying the bandwidth of the equations to solve [25].

For the special case of a symmetric geometry in the $x_1 - x_2$ plane, $L_2/L_1 = 1.0$ and $w_1^o = 1.0$, symmetric loading in the $x_1 - x_2$ plane, $\kappa_1 = 1.0$, and material properties with $\theta_0 = 45^o$ the same unit cell, Fig. 1, and boundary conditions, Eq. (13), are sufficient. This follows from the fact that considering the full, eight times larger unit cell, both geometry, the loading

and the material properties posses four-fold symmetry about the four planes $x_1 = 0, x_2 = 0, x_1 = x_2$ and $x_1 = -x_2$, and then also the solutions have these symmetries. A few results will be presented for this when $w_1^o = w_3^o = \kappa_1 = \kappa_3 = 1.0$ (spherical cavity under hydrostatic load).

The problem has been solved using an updated Lagrangian formulation [19, 26] based on the principle of virtual work in terms of the Kirchhoff stress, $\tau_{ij} = \tau_{ji}$, [27]

$$\Delta t \int_V \left( \overset{\nabla}{\tau}_{ij}\, \delta D_{ij} - \sigma_{ij}(2D_{ik}\delta D_{kj} - L_{kj}\delta L_{ki}) \right) \mathrm{d}V = \Delta t \int_S \dot{T}_i \delta \dot{u}_i \mathrm{d}S - \left[ \int_V \sigma_{ij}\delta D_{ij}\mathrm{d}V - \int_S T_i \delta \dot{u}_i \mathrm{d}S \right] \tag{15}$$

where $V$ is the volume and $S$ is the surface, $T_i = \sigma_{ij} n_j$ are the tractions, $\delta D_{ij}$, $\delta L_{ij}$ and $\delta \dot{u}_i$ are the virtual strains, velocity gradients and velocities, respectively, all referred to the current deformed configuration. The bracketed terms in Eq. (15) vanish if the current state satisfies equilibrium. However, due to numerical errors the solution tends to drift away from the true equilibrium path, and including the bracketed terms in Eq. (15) as an additional load term, prevents such drifting.

For the numerical finite element solution the cell is discretisized using iso-parametric, quadratic 20-node brick elements with three translational degrees of freedom per node. Reduced $2 \times 2 \times 2$ Gauss integration is adopted. Fig. 2 shows an example of a mesh. The elements are stretched, such that the elements are smaller near the cavity, but still fairly elongated in the radial direction. This will accommodate the large deformations expected while the cavity expands.

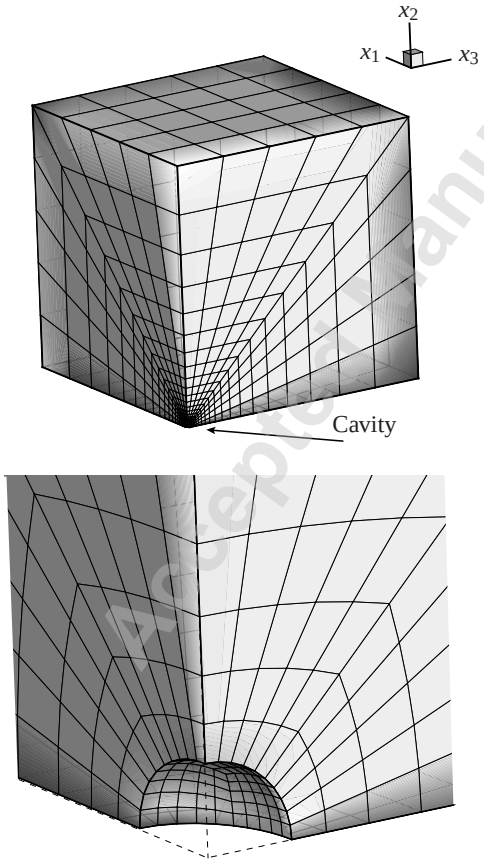


Fig. 2. Example of mesh for spheroidal cavity. A zoom of the mesh near the cavity is also shown.

Once the cavitation instability starts the remote load and/or displacement increment may become negative. Here, the combined finite element and Rayleigh-Ritz procedure in [23], makes it possible to follow the equilibrium path during such instability.

## 4 Numerical Results

Two different plastic anisotropies labeled II and IV, previously studied in [28] using Hill-48, are considered here. They are related to the experiments by Moen et al. [29] on aluminum alloy as previously discussed by the authors [6]. The coefficients of plastic anisotropy used in Eq. (6) are

| | $\bar{a}$ | $\bar{b}$ | $\bar{c}$ | $\bar{f} = \bar{g} = \bar{h}$ |
|---|---|---|---|---|
| Isotropy | 1.000 | 1.000 | 1.000 | 1.000 |
| II | 0.265 | 1.355 | 0.525 | 0.906 |
| IV | 2.072 | 0.886 | 1.105 | 2.173 |

Furthermore, two exponents will be considered, i.e. $d = 8$ and $d = 14$, see Eq. (4). The coefficients are obtained by fitting Barlat-91 with $d = 8$ to the initial yield stresses in three selected uniaxial tensile tests ($0^o, 45^o$ and $90^o$) as well as the Lankfords r-value (ratio of width to thickness plastic strains) in the $0^o$-direction. The latter then represents the slope of the yield surface in the point of uniaxial tension in the $0^o$-direction. The yield surfaces are presented in Fig. 3(a) together with the angular variation of the yield stress for the $x_1$-direction in Fig. 3(b). For anisotropy II the smallest yield stress is at $\theta = 0^o$, whereas the smallest yield stress for anisotropy IV is for $\theta \simeq 50^o$. It is noted, that the angular yield stress variation in the primary loading direction, the $x_2$-direction, is similar to that of the $x_1$-direction, but simply mirrored about $\theta_0 = 45^o$. Thus, the smallest uniaxial yield stress in the $x_2$-direction is at $\theta_0 = 90^o$ for anisotropy II and $\theta_0 \simeq 40^o$ for anisotropy IV. The three yield stresses used for calibration are marked by open circles in Fig. 3(b). For comparison Fig. 3(a) shows the two anisotropies represented by Hill-48 as well. It is clearly seen, that both Barlat-91 and Hill-48 intersect the same point at the two axes, reflecting the yield stresses in $0^o$ and $90^o$. It is also seen (most easily for anisotropy II) that the slope of the yield surfaces are the same at $\sigma_{22} = 0$ reflecting the same Lankford r-value in the $0^o$-direction. Similarly, for $\sigma_{11} = 0$ the slope of Hill-48 is clearly lower than that of Barlat-91, as Lankfords r-value in the $90^o$-direction has not been used for calibration. For $d = 14$ a small deviation is seen at the points of intersection. This is due to the fact, that the parameter estimation for Barlat-91 is based on $d = 8$ but the yield surface is shown with the same values for $d = 14$. Lastly, the isotropic Mises yield surface and the isotropic Tresca-like ($d = 20$) are shown. For the isotropic cases no angular yield stress varia-

Journal of Applied Mechanics. Received July 10, 2019;
Accepted manuscript posted September 20, 2019. doi:10.1115/1.4044955


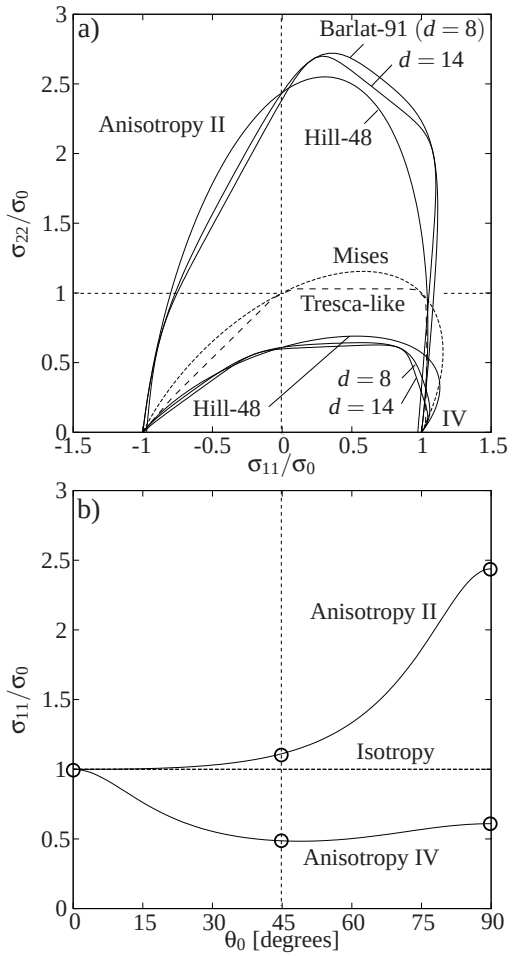


Fig. 3. Different initial yielding behavior. a) Initial yield surfaces shown in the $(\sigma_{11}, \sigma_{22})$-plane for $\sigma_{33} = \sigma_{12} = \sigma_{13} = \sigma_{23} = 0$. Two different anisotropies represented by Hill-48 and Barlat-91 (with $d = 8$ and $d = 14$) are shown together with a Tresca-like ($d = 20$) isotropic yield surface and the isotropic Mises yield surface. b) The corresponding angular uniaxial yield stress variations for Barlat-91 ($d = 8$) and isotropy.

tion is seen, Fig. 3(b).

Results are presented for the material parameters $\sigma_0/E = 0.002, \nu = 1/3, \dot{\varepsilon}_0 = 0.001\ \mathrm{s}^{-1}$, $m = 0.01$ and $n = 0.1$. The effect of the rate-sensitivity parameter, $m$, is a lowered stress level for lower values of $m$ [6]. Curves of normalized macroscopic average true stress in the $x_2$-direction, $\Sigma_2/\sigma_0$, versus the normalized current cavity volume, $V/V_0$, will be shown. The initial cavity volume is denoted $V_0$ and all computations are aborted at $V/V_0 = 60$. The current cavity volume, $V$, is found by numerical integration of the volume of the cavity. The average true stresses on the sides of the domain analyzed are computed by integration of surface tractions, such that the primarily stress, $\Sigma_2$, is

$$\Sigma_2 = \frac{1}{L_1 L_3} \int_0^{L_1} \int_0^{L_3} [T_2]_{x_2 = L_2} \mathrm{d}x_1 \mathrm{d}x_3 \qquad (16)$$

where $S$ is the surface in the current deformed geometry. The stress triaxiality, $T$, can then be defined as

$$T = \frac{\Sigma_h}{\Sigma_e} = \frac{\Sigma_1 + \Sigma_2 + \Sigma_3}{3\Sigma_e} = \frac{1}{3}(\kappa_1 + 1 + \kappa_3)\frac{\Sigma_2}{\Sigma_e} \qquad (17)$$

with the effective stress taken as $\Sigma_e = \max(|\Sigma_2 - \Sigma_1|, |\Sigma_1 - \Sigma_3|, |\Sigma_2 - \Sigma_3|)$. Very high triaxialities are required for cavitation instability to occur. The first results (Figs. 4-7) will focus on the stress ratios $\kappa_1 = \kappa_3 = 0.9$ giving a triaxiality of $T = 28/3$. Results of pure hydrostatic load, $\kappa_1 = \kappa_3 = 1.0$, giving an infinitely high triaxiality are shown in Figs. 8-10.

Fig. 4 shows the case of an initially spherical cavity, $w_1^o = w_3^o = 1.0$, represented by Barlat-91 with $d = 8$ in Eq. (4), by Hill-48 and by the isotropic Mises and Tresca-like yield surfaces. The curves for Hill-48 and Mises are repeated from [6] and the results of Mises serve as a reference case throughout the paper. Fig. 4(a) gives the normalized overall true stress, $\Sigma_2/\sigma_0$, as function of the evolving normalized cavity volume, $V/V_0$. For a cavity volume larger than approximately 10 times the initial cavity volume, $V/V_0 \gtrsim 10$, an almost constant stress level is obtained for all cases. This indicates an unstable growth of the cavity driven by the stored elastic energy in the material. For the isotropic results of the Mises and Tresca-like yield surfaces, the stress plateaus are $\Sigma_2/\sigma_0 \simeq 6.51$ and $\Sigma_2/\sigma_0 \simeq 6.46$, respectively, such that the Tresca-like yield surface results in a marginally smaller maximum stress. The effect of representing the plastic anisotropy either by Hill-48 or Barlat-91 is seen to be vanishing small, as the maximum stress for anisotropy II is $\Sigma_2/\sigma_0 \simeq 8.28$ and $\Sigma_2/\sigma_0 \simeq 8.31$, respectively, and for anisotropy IV the maximum stress by Hill-48 or Barlat-91 is $\Sigma_2/\sigma_0 \simeq 4.08$ and $\Sigma_2/\sigma_0 \simeq 4.06$, respectively. As for the isotropic results no significant difference in stress level is seen. Figs. 4(b) and (c) provide the corresponding evolutions in the cavity shape described by $w_1 = a_2/a_1$ and $w_3 = a_2/a_3$. As expected, the initial spherical cavity remains spherical for the two isotropic cases, but with a small numerical deviation between the Mises and Tresca-like yield surfaces. A much larger effect is, however, seen for anisotropy II, where the Hill-48 representation predicts both a larger $w_1$ and a larger $w_3$ compared to Barlat-91. The values for Hill-48 and Barlat-91 at $V/V_0 = 60$ are $w_1 = 1.34$ and $w_1 = 1.22$, respectively, as well as $w_3 = 1.32$ and $w_3 = 1.19$, respectively. For anisotropy IV the differences between the Hill-48 and Barlat-91 representations are smaller. At $V/V_0 = 60$ the values are $w_1 = 0.78$ and $w_1 = 0.82$ for Hill-48 and Barlat-91, respectively, whereas $w_3 = 0.98$ and $w_3 = 1.01$ for Hill-48 and Barlat-91, respectively. Hence, similarly to isotropy, the cavity of anisotropy IV expands equally in the $x_2$- and $x_3$-directions.

Fig. 5 shows the same case as in Fig. 4, i.e, $w_1^o = w_3^o = 1.0$ and Barlat-91 with $d = 8$ in Eq. (4), but a higher exponent is also considered, $d = 14$. In Fig. 5(a) it is seen, that the normalized overall true stress, $\Sigma_2/\sigma_0$, is practically unaffected by $d$. This holds for both anisotropies. However, studying the cavity shape reveals a strong effect of

Journal of Applied Mechanics. Received July 10, 2019;
Accepted manuscript posted September 20, 2019. doi:10.1115/1.4044955


$d$ for anisotropy II, as a smaller value of both $w_1$ and $w_3$ is obtained for $d = 14$. At $V/V_0 = 60$ one has $w_1 = 1.22$ for $d = 8$, but only $w_1 = 1.12$ for $d = 14$ as well as $w_3 = 1.19$ for $d = 8$, but only $w_3 = 1.10$ for $d = 14$. For anisotropy IV $w_1$ shows a visible effect of $d$, but $w_3$ seems to remain almost constantly near unity in the load range investigated.

Fig. 6 shows cases similar to those illustrated in Fig. 5 but for cavities having the initial shapes similar to the expected final shapes, i.e $w_1^o = w_3^o = 1.2$ for anisotropy II and $w_1^o = 0.85$ and $w_3^o = 1.0$ for anisotropy IV (see Fig. 5). Results for both $d = 8$ and $d = 14$ are shown. The macroscopic stress level is hardly affected by these different initial cavity shapes or values of $d$, Fig. 6(a). As expected, it can be seen from Fig. 6(b) and Fig. 6(c) that the curves for anisotropy IV are fairly flat indicating that the final shape of the cavity is similar to the initial one. However, for anisotropy II a tendency towards slightly larger final $w_1$ and $w_3$ values compared to the initial ones, i.e. $w_1 \simeq 1.35 > w_1^o = 1.2$ and $w_3 \simeq 1.32 > w_3^o = 1.2$. It is also seen, that the change in $w_1$ and $w_3$ continues all the way up to $V/V_0 \simeq 30$, whereas nearly constant values of $w_1$ and $w_3$ were obtained much earlier for initially spherical cavities, Fig. 5(b) and Fig. 5(c). The effect of $d$ is vanishing small even for anisotropy II, which showed a large effect in Fig. 5.

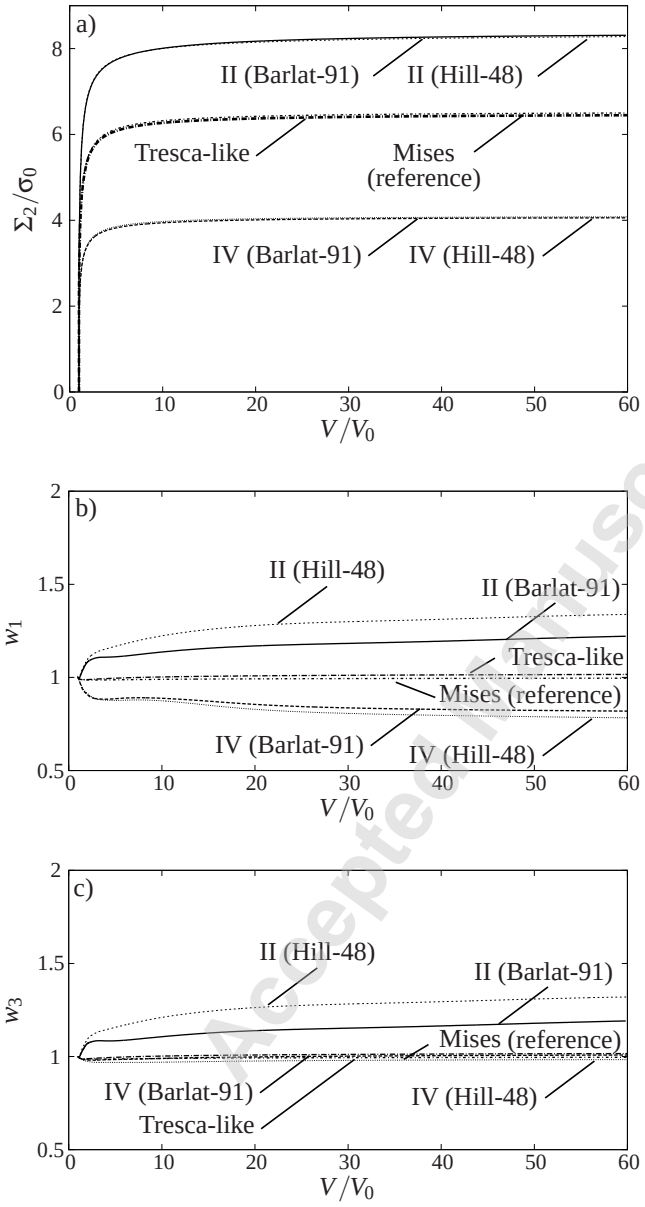


Fig. 4. Effect of initial yield surfaces when an initially spherical cavity, $w_1^o = w_3^o = 1.0$, is loaded by $\kappa_1 = \kappa_3 = 0.9$. Isotropic Mises reference curve is shown for comparison. (a) Normalized stress in the primary load direction versus current normalized cavity volume. (b) Evolution of $w_1$. (c) Evolution of $w_3$.

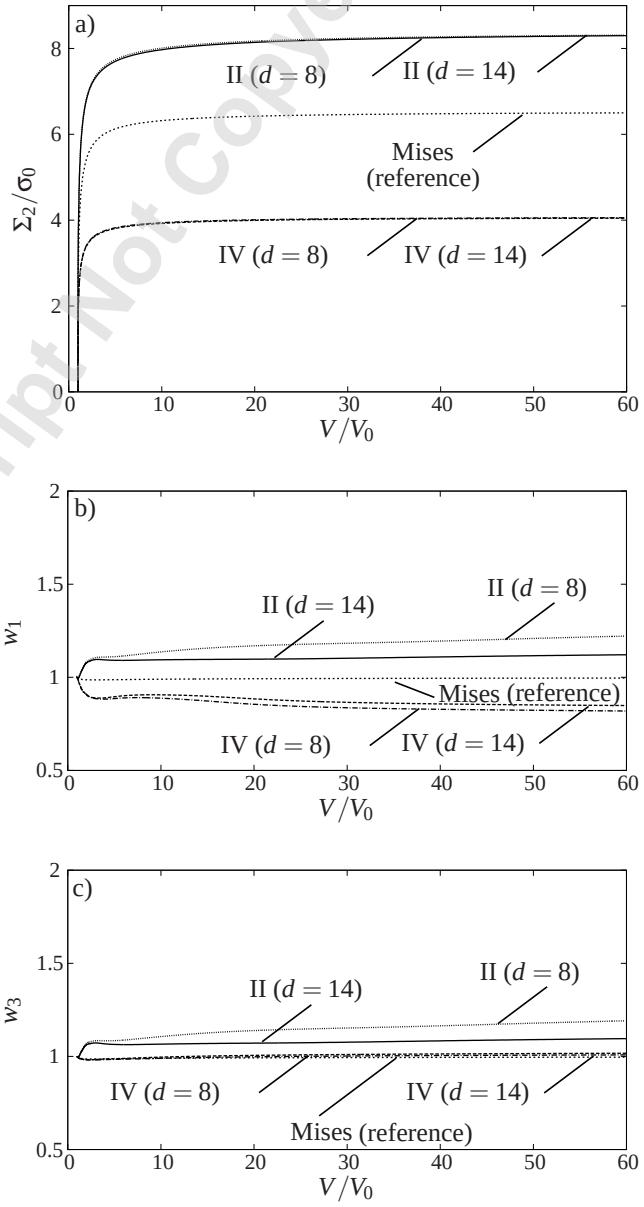


Fig. 5. Effect of yield surface exponent in Barlat-91, $d$ in Eq. (4), when an initially spherical cavity, $w_1^o = w_3^o = 1.0$, is loaded by $\kappa_1 = \kappa_3 = 0.9$. Isotropic Mises reference curve is shown for comparison. (a) Normalized stress in the primary load direction versus current normalized cavity volume. (b) Evolution of $w_1$. (c) Evolution of $w_3$.

Journal of Applied Mechanics. Received July 10, 2019;
Accepted manuscript posted September 20, 2019. doi:10.1115/1.4044955


As described in Sec. 3 the one-eighth cell used here is capable of handling other initial orientation, $\theta_0$, of plastic anisotropy, Fig. 1, than that of $\theta_0 = 0^o$. For $d = 8$ Fig. 7 shows results for $\theta_0 = 90^o$ in comparison with the previous results for $\theta_0 = 0^o$. The stress curves in Fig. 7(a) show very little influence of $\theta_0$, but the cavity shape is very much affected, Fig. 7(b) and Fig. 7(c). For anisotropy II with $\theta_0 = 0^o$ $w_1 \simeq 1.22$ and $w_3 \simeq 1.19$ but for $\theta_0 = 90^o$ $w_1 \simeq 0.69$ and $w_3 \simeq 0.98$. Hence, the cavity is elongated in the $x_2$-direction for $\theta_0 = 0^o$ while for $\theta_0 = 90^o$ the cavity is elongated in the $x_1$-direction. For anisotropy IV the cavity is elongated in the $x_1$-direction for $\theta_0 = 0^o$ while for $\theta_0 = 90^o$ the cavity is elongated in the $x_2$-direction. This agrees with the expectations, as $\theta_0 = 90^o$ effectively means interchanging the $x_1$- and $x_2$-axes, see Fig. 1. It is also noted, that completely by chance, the evolutions of $w_1$ and $w_3$ for anisotropy II with $\theta_0 = 0^o$ are quite similar to anisotropy IV with $\theta_0 = 90^o$ and that $w_3$ for anisotropy II with $\theta_0 = 90^o$ is very similar to anisotropy IV with $\theta_0 = 0^o$. Results for $d = 14$ for both anisotropies show only a minor difference from those with $d = 8$ in Fig. 7. This holds true for both the macroscopic stresses as well as the cavity shapes. Therefore, these results will not be shown here.

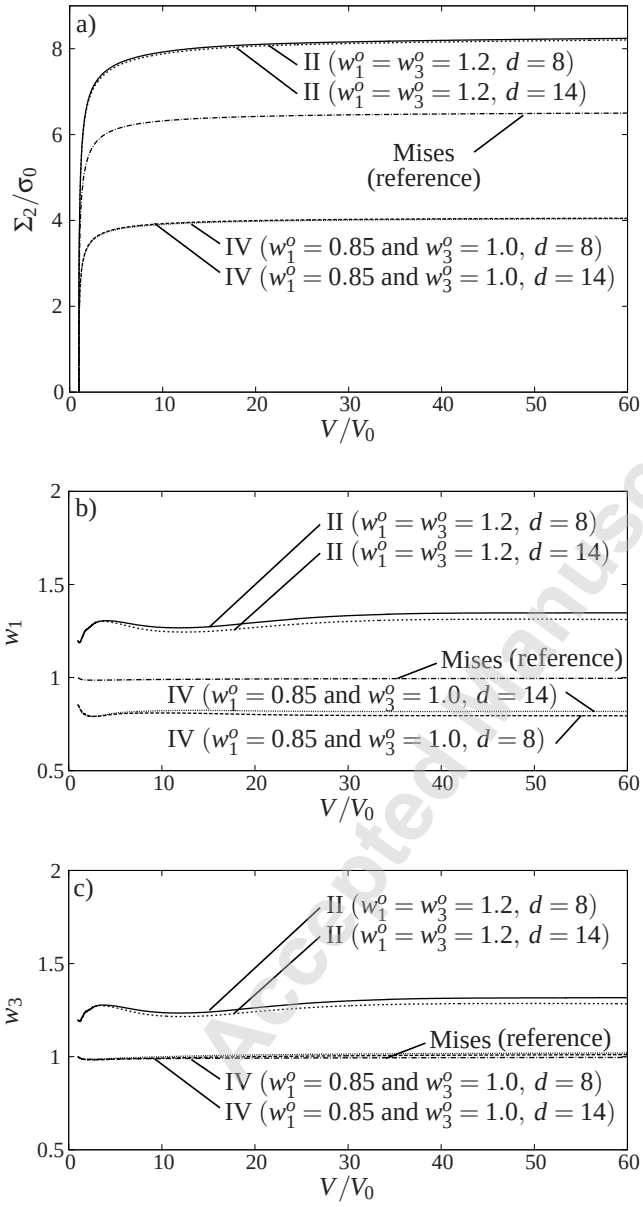


Fig. 6. Effect of initial cavity shapes, $w_1^o$ and $w_3^o$, for Barlat-91 when loaded by $\kappa_1 = \kappa_3 = 0.9$. Isotropic Mises reference curve is shown for comparison. (a) Normalized stress in the primary load direction versus current normalized cavity volume. (b) Evolution of $w_1$. (c) Evolution of $w_3$.

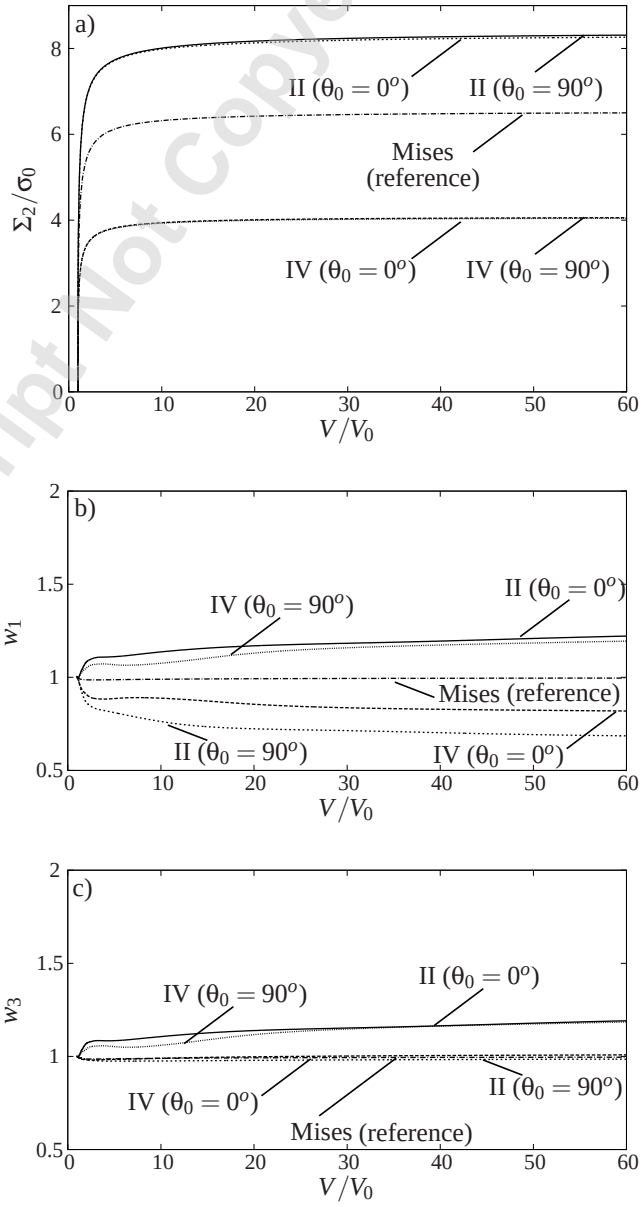


Fig. 7. Effect of initial orientation of plastic anisotropy, $\theta_0$, when an initially spherical cavity, $w_1^o = w_3^o = 1.0$, is loaded by $\kappa_1 = \kappa_3 = 0.9$. Isotropic Mises reference curve is shown for comparison. (a) Normalized stress in the primary load direction versus current normalized cavity volume. (b) Evolution of $w_1$. (c) Evolution of $w_3$.

Journal of Applied Mechanics. Received July 10, 2019;
Accepted manuscript posted September 20, 2019. doi:10.1115/1.4044955


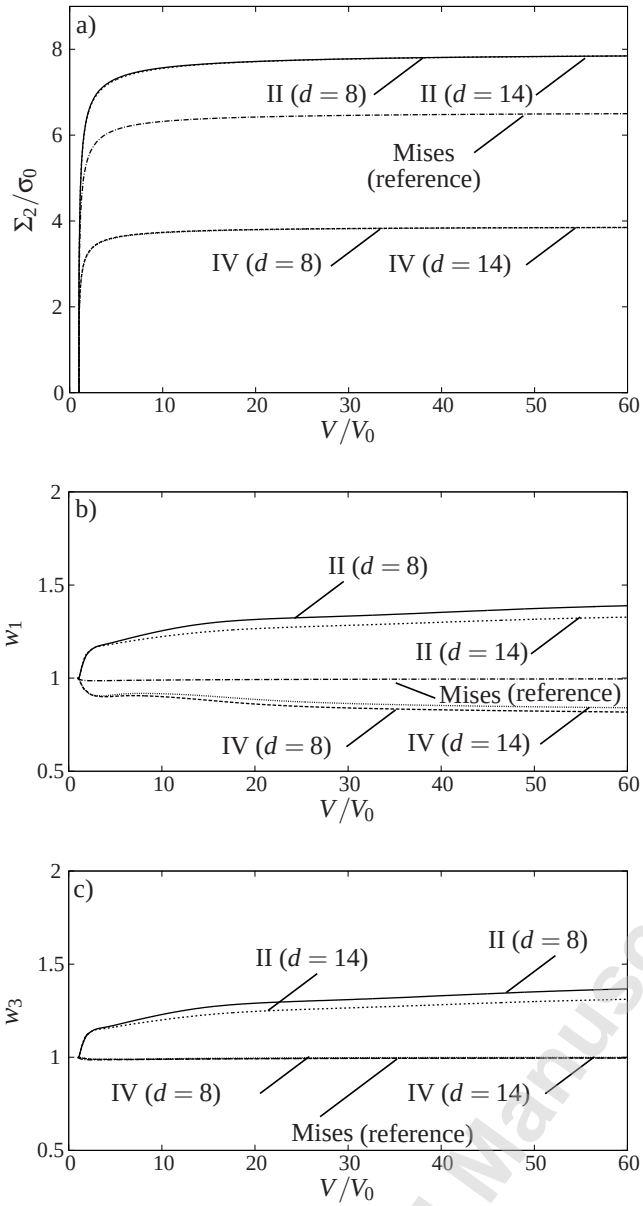


Fig. 8. Effect of yield surface exponent in Barlat-91, $d$ in Eq. (4), when an initially spherical cavity, $w_1^o = w_3^o = 1.0$, is loaded by $\kappa_1 = \kappa_3 = 1.0$. Isotropic Mises reference curve is shown for comparison (with $\kappa_1 = \kappa_3 = 0.9$). (a) Normalized stress in the primary load direction versus current normalized cavity volume. (b) Evolution of $w_1$. (c) Evolution of $w_3$.

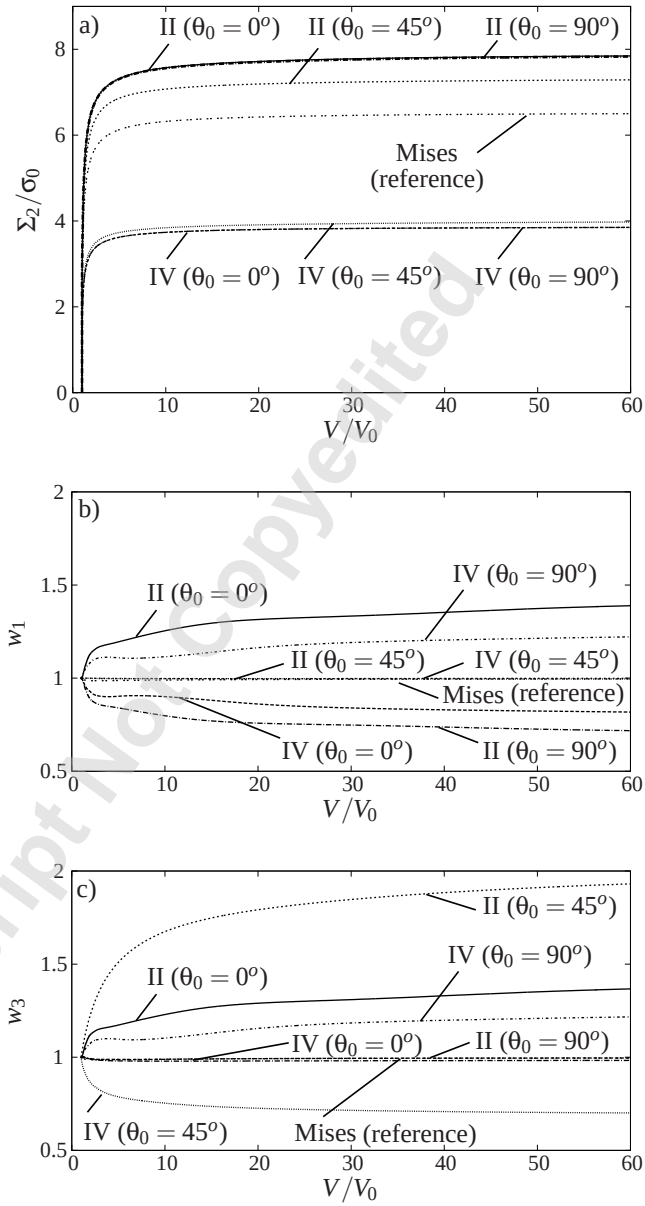


Fig. 9. Effect of initial orientation of plastic anisotropy, $\theta_0$, when an initially spherical cavity, $w_1^o = w_3^o = 1.0$, is loaded hydrostatically, $\kappa_1 = \kappa_3 = 1.0$. Isotropic Mises reference curve is shown for comparison (with $\kappa_1 = \kappa_3 = 0.9$). (a) Normalized stress in the primary load direction versus current normalized cavity volume. (b) Evolution of $w_1$. (c) Evolution of $w_3$.

For $\kappa_1 = \kappa_3 = 1.0$ a hydrostatic load is applied and the triaxiality, $T$ in Eq. (17), is not defined as the effective stress in the denominator is zero ($T$ is approaching infinity). The remaining results will focus on this load case for an initially spherical cavity, $w_1^o = w_3^o = 1.0$.

Fig. 8 shows the effects of two different values of the exponent in Eq. (4) for $\theta_0 = 0^o$, see also Fig. 5. The macroscopic stress plateau of Fig. 8(a) is slightly lowered at this higher triaxiality, but still unaffected by the value of the exponent $d$. For anisotropy II the stress level reduces from $\Sigma_2/\sigma_0 \simeq 8.31$ to $\Sigma_2/\sigma_0 \simeq 7.85$ and for anisotropy IV from $\Sigma_2/\sigma_0 \simeq 4.06$ to $\Sigma_2/\sigma_0 \simeq 3.85$. The higher triaxiality causes the cavity to deform more severely. As also seen for $\kappa_1 = \kappa_3 = 0.9$ in Fig. 5 a large growth in both $w_1$ and $w_3$ is seen for anisotropy II from the very beginning, but now the growth does not stagnate as early as for anisotropy II with $d = 14$ in Fig. 5. Under the hydrostatic load the growth in both $w_1$ and $w_3$ for anisotropy II continues throughout the load range considered here, such that the shape at $V/V_0 = 60$ is given by $w_1 \simeq 1.39$ and $w_3 \simeq 1.37$ for $d = 8$ and slightly lower for $d = 14$. Most likely, the final shape parameters are marginally higher than this, but the computations have not

Journal of Applied Mechanics. Received July 10, 2019;
Accepted manuscript posted September 20, 2019. doi:10.1115/1.4044955


been continued further to obtain these values. For anisotropy IV the difference between $d = 8$ and $d = 14$ is small and the evolution in both $w_1$ and $w_3$ has saturated at $V/V_0 \simeq 30$.

Fig. 9 shows results for different values of the initial orientation of plastic anisotropy, given by $\theta_0$, see Fig. 1. As a hydrostatic load is introduced remotely for a spherical cavity, the special case of $\theta_0 = 45^o$ can also be analyzed as discussed previously. The macroscopic stress level reaches the same value for $\theta_0 = 0^o$ and $\theta_0 = 90^o$, i.e. $\Sigma_2/\sigma_0 \simeq 7.84$ for anisotropy II and $\Sigma_2/\sigma_0 \simeq 3.85$ for anisotropy IV, Fig. 9(a). As discussed in relation to Fig. 3(b) the yield stress for uniaxial tension in the primary loading direction, the $x_2$-direction, is a simple mirroring around $\theta_0 = 45^o$ of the curves in Fig. 3(b). Thus, the yield stress for $\theta_0 = 45^o$ decreases for anisotropy II but slightly increases for anisotropy IV. For $\theta_0 = 45^o$ with anisotropy II the stress plateau in Fig. 9(a) also decreases to $\Sigma_2/\sigma_0 \simeq 7.29$, whereas it increases only slightly for anisotropy IV to $\Sigma_2/\sigma_0 \simeq 3.98$ . It is, however, not at all a uniaxial stress state in Fig. 9, and the large differences seen in Fig. 3 for both anisotropies when $\theta_0 = 0^o$ and $\theta_0 = 90^o$, are apparently not affecting the macroscopic stress levels.

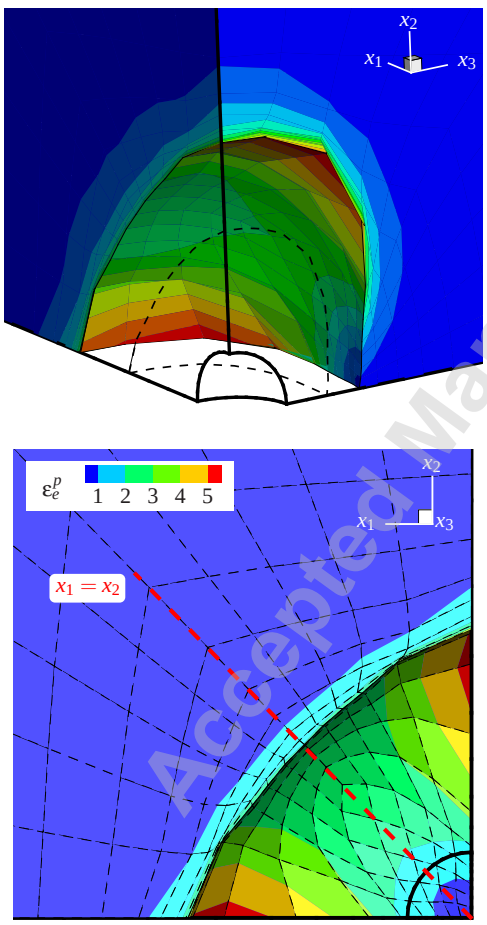


Fig. 10. Initial and deformed geometries with contours of effective plastic strain, $\varepsilon^p$ in Eq. (10), for anisotropy II with $\theta_0 = 45^o$ and an initial cavity shape of $w_1^o = w_3^o = 1.0$, loaded by $\kappa_1 = \kappa_3 = 1.0$, see also Fig. 9. a) $V/V_0 \simeq 15$ (black dashed line) and $V/V_0 \simeq 46$ with contours. b) $V/V_0 \simeq 46$ with contours in $x_1 - x_2$ plane.

Studying the evolution of the cavity shapes through $w_1$ and $w_3$, Fig. 9(b) and Fig. 9(c), clearly shows that the $\theta_0 = 45^o$ cases deform in the same manner in the $x_1$- and $x_2$-directions as $w_1 = a_2/a_1$ remains constantly unity throughout the load history, Fig. 9(b). This is not the case for $w_3 = a_3/a_1$ in Fig. 9(c). For anisotropy II $w_3$ grows to $w_3 \simeq 1.93$ (the cavity turns into an oblate in the $x_1 - x_2$-plane). For anisotropy IV $w_3$ decreases to $w_3 \simeq 0.70$ (the cavity turns into a prolate in the $x_1 - x_2$-plane). In all cases the mesh becomes rather distorted in the radial direction, where the surface elements become very thin, but for the anisotropic cases the distortion is more pronounced. For two different levels of deformation corresponding to $V/V_0 \simeq 15$ and $V/V_0 \simeq 46$ in Fig. 9, the deformed cavities for anisotropy II are shown in Fig. 10. For $V/V_0 \simeq 15$ only the deformed geometry is shown by the dashed line in Fig. 10(a), but for $V/V_0 \simeq 46$ contours of effective plastic strain, $\varepsilon^p$ in Eq. (10), are included as well. Fig. 10(b) shows the results in the $x_1 - x_2$ plane for $V/V_0 \simeq 46$ only. The oblate shaped cavity is clearly seen when shown in perspective, Fig. 10(a), and the symmetric deformation field in the $x_1 - x_2$-plane around the $x_1 = x_2$ plane (red dashed line in Fig. 10(b)) is also recognized from the deformed mesh shown by black dashed lines in Fig. 10(b). At the surface of the cavity very large plastic deformations occur, but rapidly the magnitude decays away from the cavity. It is noted that the evolution of the cavity shape is given for cases by $w_1$ and $w_3$ in the sub-figures (b) and (c) of Figs. 4-9.

## 5 Discussion

Full detailed 3D numerical analyses of cavitation instability have been conducted in order to investigate the influence of a non-quadratic anisotropic yield surface denoted Barlat-91.

A cavitation instability happens at very high stress triaxialities and the current work focuses on a triaxiality close to hydrostatic tension and full hydrostatic tension. Previous work on cavitation instability has assumed isotropy or in few cases anisotropic plasticity in which the stresses enter quadratically through a yield surface, such as Hill-48.

Two sets of plastic anisotropies have been investigated here and they are labeled II and IV. All computations have been truncated when in the initial volume of the cavity has increased a factor of 60. However, in most cases the critical stress level at instability has been reached much sooner. The critical stress is found to be highest for anisotropy II and lowest for anisotropy IV. This is in accordance with previous finding of the authors using Hill-48 and a direct comparison shows that essentially the same stress level is predicted if Hill-48 or Barlat-91 with two different exponents are adopted. Even if the principal axes of anisotropy is rotated $90^o$ the stress level remains nearly the same. If full hydrostatic tension is considered a slightly reduced stress level is observed. For a $45^o$ rotation of the principal axes of anisotropy the stress level reduces by 7% for anisotropy II, Fig. 9.

The shape of the cavity has been investigated as well. The effect of Barlat-91 versus the classical Hill-48 is a less

Journal of Applied Mechanics. Received July 10, 2019;
Accepted manuscript posted September 20, 2019. doi:10.1115/1.4044955


profound cavity elongation for Barlat-91, Fig. 4. Anisotropy II shows this effect most clearly. Generally, anisotropy II seems to be more affected by the difference between the two exponents considered. For the $45^o$ rotation under full hydrostatic tension it was confirmed, that the cavity expands the same amount in the two directions of the plane perpendicular to the axis of rotation, Fig. 10, as follows from the symmetry about the $x_1 = x_2$ plane.

**References**

[1] Bishop, R. F., Hill, R., and Mott, N. F., 1945. "The theory of indentation and hardness tests". *Proceedings of the Physical Society of London*, **57**(321), pp. 147–159.

[2] Hill, R., 1950. *The Mathematical Theory of Plasticity*. The Clarendon Press, Oxford.

[3] Huang, Y., Hutchinson, J. W., and Tvergaard, V., 1991. "Cavitation instabilities in elastic plastic solids". *Journal of the Mechanics and Physics of Solids*, **39**(2), pp. 223–241.

[4] Tvergaard, V., Huang, Y., and Hutchinson, J. W., 1992. "Cavitation instabilities in a power hardening elastic-plastic solid". *European Journal of Mechanics A-solids*, **11**(2), pp. 215–231.

[5] Tvergaard, V., and Hutchinson, J. W., 1993. "Effect of initial void shape on the occurrence of cavitation instabilities in elastic-plastic solids". *Journal of Applied Mechanics-transactions of the ASME*, **60**(4), pp. 807–812.

[6] Tvergaard, V., and Legarth, B., 2019. "Effects of anisotropy and void shape on cavitation instabilities". *International Journal of Mechanical Sciences*, **152**, pp. 81–87.

[7] Dalgleish, B. J., Trumble, K. P., and Evans, A. G., 1989. "The strength and fracture of alumina bonded with aluminum-alloys". *Acta Metallurgica*, **37**(7), pp. 1923–1931.

[8] Flinn, B. D., Rühle, M., and Evans, A. G., 1989. "Toughening in composites of $Al_2O_3$ reinforced with Al". *Acta Metallurgica*, **37**(11), pp. 3001–3006.

[9] Ashby, M. F., Blunt, F. J., and Bannister, M., 1989. "Flow characteristics of highly constrained metal wires". *Acta Metallurgica*, **37**(7), pp. 1847–1857.

[10] Tvergaard, V., 2016. "Cavitation instabilities between fibres in a metal matrix composite". *Acta Mechanica*, **227**(4), pp. 993–1003.

[11] Ball, J. M., 1982. "Discontinuous equilibrium solutions and cavitation in nonlinear elasticity". *Philosophical Transactions of the Royal Society of London a (mathematical and Physical Sciences)*, **306**(1496), pp. 557–611.

[12] Horgan, C. O., and Abeyaratne, R., 1986. "A bifurcation problem for a compressible nonlinearly elastic medium - growth of a micro-void". *Journal of Elasticity*, **16**(2), pp. 189–200.

[13] Horgan, C. O., and Polignone, D. A., 1995. "Cavitation in nonlinearly elastic solids: A review". *Applied Mechanics Reviews*, **48**(8), p. 471.

[14] Hill, R., 1948. "A theory of the yielding and plastic flow of anisotropic metals". *Proceedings of the Royal Society of London*, **A193**, pp. 281–297.

[15] Barlat, F., Lege, D. J., and Brem, J. C., 1991. "A six-component yield function for anisotropic materials". *International Journal of Plasticity*, **7**, pp. 693–712.

[16] Dafalias, Y. F., 1985. "A missing link in the macroscopic constitutive formulation of large plastic deformation". In Plasticity Today, Modelling, Methods and Applications, A. Sawczuk and G. Bianchi, eds., Elsevier, Amsterdam, pp. 135–151.

[17] Dafalias, Y. F., 1985. "The plastic spin". *Transactions of the ASME. Journal of Applied Mechanics*, **52**(4), pp. 865–871.

[18] Dafalias, Y. F., 1993. "On multiple spins and texture development. Case study: kinematic and orthotropic hardening". *Acta Mechanica*, **100**, pp. 171–194.

[19] Yamada, Y., and Sasaki, M., 1995. "Elastic-plastic large deformation analysis program and lamina compression test". *International Journal of Mechanical Sciences*, **37**(7), pp. 691–707.

[20] Legarth, B. N., and Kuroda, M., 2004. "Particle debonding using different yield criteria". *European Journal of Mechanics - A/Solids*, **23**(5), pp. 737–751.

[21] Peirce, D., Shih, C. F., and Needleman, A., 1984. "A tangent modulus method for rate dependent solids". *Computers and Structures*, **18**, pp. 875–887.

[22] Kuroda, M., and Tvergaard, V., 2001. "Plastic spin associated with a non-normality theory of plasticity". *European Journal of Mechanics - A/Solids*, **20**(6), pp. 893–905.

[23] Tvergaard, V., 1976. "Effect of thickness inhomogeneities in internally pressurized elastic-plastic spherical shells". *Journal of the Mechanics and Physics of Solids*, **24**, pp. 291–304.

[24] Liu, Z. G., Wong, W. H., and Guo, T. F., 2016. "Void behaviors from low to high triaxialities: Transition from void collapse to void coalescence". *International Journal of Plasticity*, **84**, pp. 183–202.

[25] Legarth, B. N., 2004. "Unit cell debonding analyses for arbitrary orientations of plastic anisotropy". *International Journal of Solids and Structures*, **41**(26), pp. 7267–7285.

[26] McMeeking, R. M., and Rice, J. R., 1975. "Finite-element formulations for problems of large elastic-plastic deformation". *International Journal of Solids and Structures*, **11**, pp. 601–616.

[27] Legarth, B. N., 2007. "Strain-gradient effects in anisotropic materials". *Modelling and Simulation in Materials Science and Engineering*, **15**, pp. S71–S81.

[28] Legarth, B. N., and Tvergaard, V., 2010. "3D analyses of cavitation instabilities accounting for plastic anisotropy". *Zeitschrift Fuer Angewandte Mathematik Und Mechanik*, **90**(9), pp. 701–709.

[29] Moen, L. A., Langseth, M., and Hopperstad, O., 1998. "Elastoplastic buckling of anisotropic aluminum, plate elements". *Journal of Structural Engineering*, pp. 712–719.